Applied Physics A (2018) 124:88
https://doi.org/10.1007/s00339-017-1531-z

Applied Physics A
Materials Science & Processing

Effect of lattice defects on the structural and optical properties of $Ni_{1-X}Ag_XO$ (where $X = 0.0, 0.01, 0.03, 0.05, 0.10$ and 0.15) nanoparticles

Rohit Sharma[1] · **Kamlesh Yadav**[1]

Received: 8 November 2017 / Accepted: 26 December 2017

Abstract
The $Ni_{1-X}Ag_XO$ (where $X = 0$, 0.01, 0.02, 0.03, 0.05, 0.10, and 0.15) nanoparticles are synthesized by sol–gel technique. The effects of Ag-doping in NiO nanoparticle on the structural and optical properties are studied. XRD analysis confirms that the prepared samples are single phase and oxygen deficient in nature. The unit cell volume decreases with the increase in the Ag-doping content. The crystallite size decreases from 23 to 19 nm with increasing the Ag-doping content up to $X = 0.10$. The strain increases with increase in Ag-doping concentration. FESEM analysis confirms that the pure sample of NiO is quasi-spherical and this shape is deformed as the Ag content increases in the NiO samples. The increase in the agglomeration of nanoparticles with the increase in doping content is also observed. UV–Visible analysis shows that the calculated optical band gap of the pure NiO sample is 3.70 eV which is less than the reported value 4.42 eV of NiO nanoparticles. The optical band gap increases as the Ag-doping content increases in the host NiO lattice. The change in band gap is increased rapidly for the $X = 0.01$ sample and then become slow for the rest of the samples. FT–IR analysis gives all the information regarding the functional group present in the samples. The effect of disorder created due to Ag-doping in NiO lattice leads to the formation of lattice defects and affects the structural and optical properties, which have been discussed in this paper in detail.

1 Introduction

The nanomaterials of the transition metal oxides such as TiO_2, ZnO, and Fe_2O_3 are widely studied due to their unique properties such as wide band gap, and high dielectric constant, which makes them a suitable candidate for the various technological applications [1]. The effects of particle size, doping, strain and film thickness, etc on the magnetic and optical properties of oxides nanomaterials have been reported [2–5]. Bulk nickel oxide (NiO) is deep green in color, whereas nanoparticles are black [6]. The detail electronic states and optical properties of NiO are also reported [7, 8]. The absorbance spectra of the NiO confirmed the electronic d–d excitations with energy band gap of about 3.8 eV [9]. The morphology of the NiO nanoparticles depends upon the synthesis conditions [10]. It is reported that the optical band gap of NiO nanoparticles increases as the particle size decreases [11–15]. The lattice parameter and specific surface area also increase with the decrease in the particle size [12, 14]. The doped NiO nanoparticles can be used in the different applications like in solar cell [16], gas sensor [17], supercapacitors [18], antibacterial and catalytic activity [19, 20], lithium-ion batteries [21], and in optoelectronic devices.

Nickel oxide had the face-centered cubic structure similar to rock salt structure of NaCl [22] and lattice constant of 4.1684 Å [23, 24]. The computer simulation of NiO shows the significance of Ni^{3+} for the stabilization of NiO [25]. Nickel oxide is the p-type semiconductor with band gap 3.6 to 4.42 eV [26] and also known as a Mott–Hubbard insulator [22], having resistivity 10^{13} Ω cm [27]. Nickel oxide can be fabricated in many crystalline phases such as cubic, and monoclinic crystals [1]. NiO nanoparticle is magnetic in nature and shows an antiferromagnetic behavior [28]. It can be synthesized by various methods such as sonochemical [29, 30], sol–gel [31–34], co-precipitation [35], microemulsion [36], and thermal decomposition [37].

The Cu doping in NiO enhances the semiconductivity [33, 38], Mg-doped NiO show increase in the band gap

✉ Kamlesh Yadav
kamlesh.yadav001@gmail.com; kamlesh_yadav@cup.ac.in; kamlesh.yadav@cup.edu.in

[1] Department of Physical Sciences, School of Basic and Applied Sciences, Central University of Punjab, Bathinda 151001, India

Published online: 09 January 2018

with the increase of Mg content [39], Li-doped NiO shows that the transmittance decreases and resistivity increases with increasing the Li doping concentration [40], Cd doping in NiO nanoparticles shows that the optical band gap increases from 2.95 to 3.95 eV with the increase in Cd-doping concentration [41], Fe-doped NiO confirms through magnetic measurement that Fe accumulate on the surface of the nanoparticles [42], and Mn doping in NiO enhances the ferromagnetic property [43]. It is also reported that the impurity doping affects the oxidation rate; monovalent atom (Li^+, Na^+) decreases the oxidation rate, whereas the trivalent impurity (Cr^{3+}, Al^{3+}) increases the rate of oxidation [44]. No doubt, the doping leads to change in the host material such as crystal distortion, defects or modify the band structure of materials. The defects and vacancies also affect the optical, structural and magnetic properties of nanomaterials. Junpeng Wang et al. reported that the oxygen vacancies influence the optical and electronic properties of the ZnO; the band gap of the material gets narrow as the oxygen vacancies are increased [45]. The electron localization is also reported as the result of linear ordering of oxygen vacancies [46].

In the present work, we have synthesized the $Ni_{1-X}Ag_XO$ (where $X = 0.0$, 0.01, 0.03, 0.05, 0.10. and 0.15) nanoparticles via sol–gel synthesis process. The effect of lattice defects produced due to Ag-doping in NiO lattice on the structural and optical properties of $Ni_{1-X}Ag_XO$ (where $X = 0.0$, 0.01, 0.03, 0.05, 0.10 and 0.15) nanoparticles have been studied in this paper in detail.

2 Experimental procedure

$Ni_{1-X}Ag_XO$ (where $X = 0.0$, 0.01, 0.03, 0.05, 0.10 and 0.15) nanoparticles were prepared with the sol–gel method [35]. In this method, 0.1 M of nickel nitrate hexahydrate ($Ni(NO_3)\cdot 6H_2O$) and 0.1 M citric acid ($C_6H_8O_7\cdot H_2O$) (Sigma Aldrich) solution were prepared. The nickel nitrate solution was added dropwise to the citric acid solution. Then, the mixed solution was heated at 70 °C for 12 h on the magnetic stir. After the gel formation, samples were dried and aged for 24 h at 110 °C. The powder obtained was sintered at 600 °C for 4 h. After sintering, the grinding was done for 1 h. The final powder after grinding was used for the various characterizations. The other samples with $X = 0.01$–0.15 were prepared by taking the dopant in stoichiometry ratio and the whole procedure was repeated. X-ray diffraction (XRD) (PAN-Analytical Xpert-Pro) was used for the structural analysis of Ag-doped samples. The morphological study was done with Field Emission Scanning Electron Microscope (FESEM) [model Merlin compact 6073, Carl Ziess]. Elemental composition of $Ni_{1-X}Ag_XO$ (where $X = 0.01$, 0.02, 0.03, 0.04, 0.05, 0.10, and 0.15) was confirmed by the energy dispersive X-ray Analyser (EDX). It is found that no impurity peaks are present in the samples and the elements Ni and Ag are present in a near stoichiometric ratio with oxygen deficiency in the prepared samples within the experimental error. UV–Visible spectrometer (Shimadzu, UV-2450) was used for the study optical properties. Fourier Transformed-Infrared (FT–IR) (400–4000 cm^{-1}) spectroscopy was done (TENSOR 27) to obtain the information of functional group attached to prepared nanoparticles.

3 Results and discussions

3.1 Xrd analysis

Figure 1 shows the X-ray diffraction (XRD) patterns of some representative $Ni_{1-X}Ag_XO$ (where $X = 0.0$, 0.05 and 0.10) samples. The peaks occurring at 37.37°, 43.40°, 62.96°, 75.48°, and 79.44° are indexed with the corresponding miller plane (111), (200), (220), (311), and (222) as per the reported literature [20, 21, 47] and the peak at 44.57° for $X = 0.0$ marked with # in Fig. 1 is of Ni having a plane (111) [48]. The small Ni peak has no effect on optical properties and it can be removed by converting the Ni into NiO by increasing the sintering temperature as reported [9]. These index peaks clearly indicate that the prepared samples have a face-centered cubic structure [23]. A very small impurity peak of Ni_2O_3 is also observed in NiO sample as also reported in [49]. Such a small amount of Ni_2O_3 also cannot affect the optical properties of the prepared NiO nanoparticles. A weak Ag (111) reflects (marked with * in Fig. 1) can be seen for the sample with $X = 0.05$ and 0.10 in Fig. 1 [50]. The Ag peak is observed because it has difficulty entering the NiO lattice; Ag^+ ions accumulate at the grain boundaries resulting in the formation of Ag clusters nanostructure. These Ag clusters inhibit the grain-growth as well as the formation of Ni and Ni_2O_3 phases [51]. The calculated lattice constant "*a*" is 4.1666 Å for NiO sample which is less than the reported value of lattice parameter 4.1684 Å [23]. This indicates that the NiO sample is oxygen deficient [52]. A decrease in the lattice constant and unit cell volume with the increase in the Ag-doping content is observed (see Table 1). Figure 1 containing the enlarged image of most intense peak also clearly shows that the peaks shift towards higher angle with the increase in Ag-doping concentration which clarifies the decrease in unit cell volume with the increase in the Ag-doping content. But, the decrease in the unit cell volume cannot be explained on the basis of ionic radii mismatch of Ag^+ and Ni^{2+} ions since the ionic radii of Ag^+ (1.15 Å) is higher than the Ni^{2+} (0.69 Å). However, it is reported in the literature that the doped metal ions with lower charge value (like Ag^+) than the host atoms (like Ni^{2+}) produce oxygen vacancies [53, 54]. The formation of O^{2-} vacancies and silver nanoclusters in lattice sites reduces the lattice parameters

Table 1 Values obtained from analysis of XRD and FESEM data of the $Ni_{1-X}Ag_XO$ (where $X=0.0$, 0.01, 0.03, 0.05, 0.10, and 0.15)

Samples of $Ni_{1-X}Ag_XO$	Crystallite Size from XRD (nm)	Particle size from FESEM (nm)	Lattice constant (Å)	Unit cell volume $(Å)^3$	Strain $\frac{\beta \cot\theta}{4}$ $(\times 10^{-3})$
$X=0$	23	52	4.1666	72.334	1.618
$X=0.05$	22	21	4.1630	72.146	1.680
$X=0.10$	19	15	4.1575	71.863	1.896

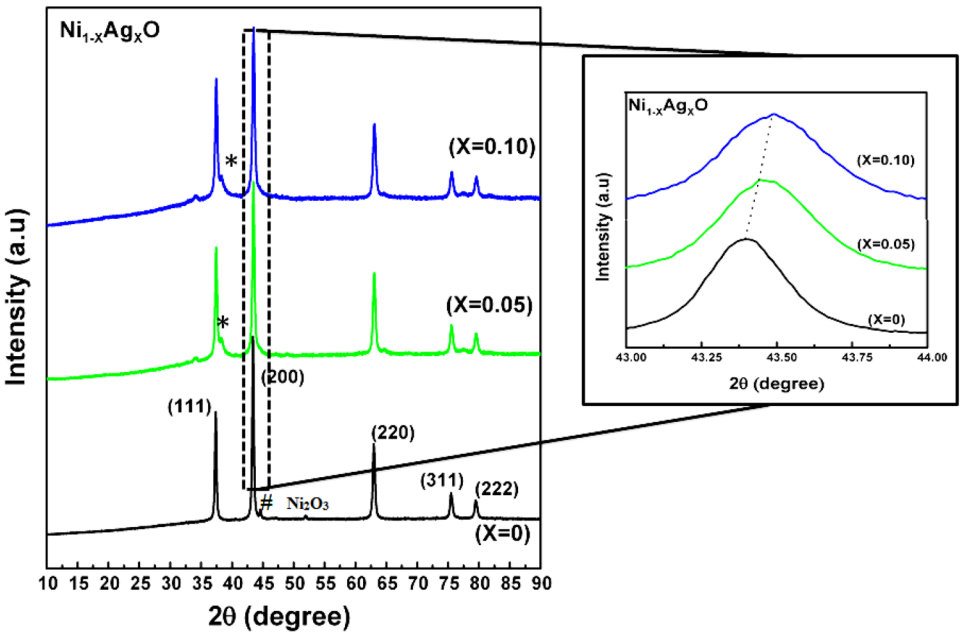

Fig. 1 XRD pattern of the $Ni_{1-X}Ag_XO$ (where $X=0.0$, 0.05, and 0.10) and the enlarged figure represents the shift in the peak toward the higher angle

as also reported in Ag-doped TiO_2 and ZnO [2, 50, 55, 56]. However, since the ionic radii of Ag^+ and Ni^{2+} are different; the substitution creates significant lattice distortion. No any other phases, such as AgO, are observed in XRD spectra.

The crystallite size is calculated through the Debye–Scherrer formula [32], $D=K\lambda/\beta \cos\theta$, where D is the crystallite size, $K=0.89$ constant known as shape factor, β is the FWHM, θ is the angle of diffraction, and λ is the wavelength of Cu kα is 1.5406 Å. The calculated values are given in Table 1. The crystallite size decreases from 23 to 19 nm with increasing the Ag-doping content up to $X=0.10$. The number of Ag ions increases on the surface of crystallite with the increase in Ag-doping concentration which inhibits the growth of NiO [41, 57, 58]. The strain is calculated by equation $\varepsilon=(\beta \cot\theta)/4$ where β is the FWHM and ε is the root-mean-square value of microstrain [59]. The values of strain are given in Table 1. The strain increases as the content of silver increases and there is an inverse relation occurring between the particle size and strain [60, 61]. This is due to the incorporation of Ag in the NiO. The substitution of every Ni^{2+} ion by Ag^+ ion converts one neighboring Ni^{2+} ion into Ni^{3+} ion to preserve the electrical neutrality in the crystal; the detailed mechanism of Ni^{3+} production has been reported in K^+-doped NiO films [62]. The production of the Ni^{3+} ions can create an intrinsic lattice defect and the formation of oxygen vacancies [63]. Hence, it leads to increase in strain with the increase in Ag-doping content.

3.2 FESEM analysis

Figure 2a–f shows the FESEM images of $Ni_{1-X}Ag_XO$ (where $X=0.0$, 0.01, 0.02, 0.03, 0.05, 0.10, and 0.15). The insets of Fig. 2a–f shows the Gaussian fitting of histogram plotted between particle size and frequency of occurrence of the particles which is used for calculating the average particle size of the present samples. It is clear from the Fig. 2 that the particles are quasi-spherical in nature. The agglomeration of the nanoparticles is increasing with the increase in the Ag-dopant concentrations. A graph is plotted between the average particle size and content of Ag (see Fig. 3). However, the average particle size decreases with increasing the concentration of the Ag. Generally, the increase in agglomeration leads to increase in average particle size, but opposite effect is observed here. In addition to this, the average particle size decreases rapidly when the X is increased from 0.0 to 0.05, however, the average

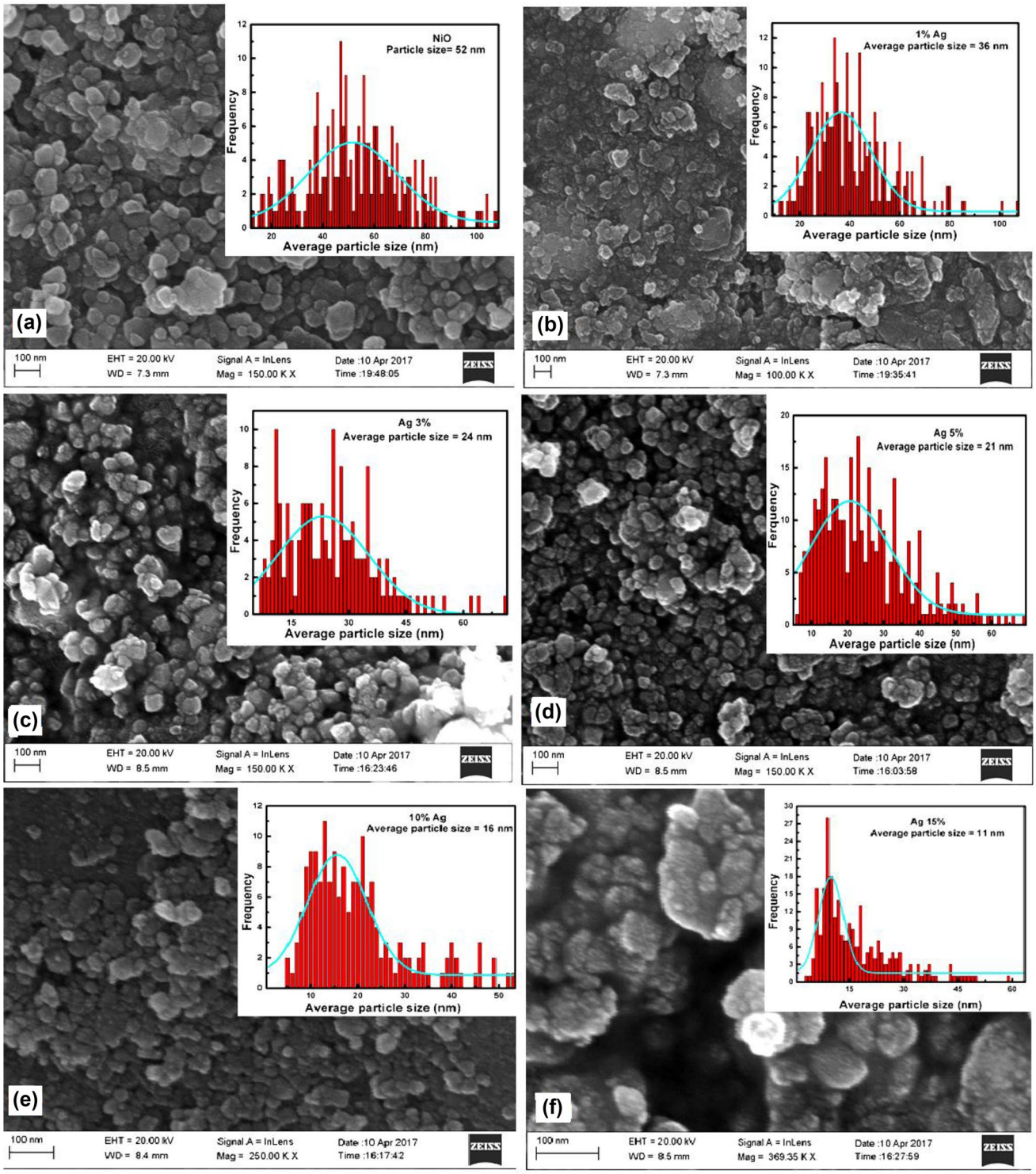

Fig. 2 **a–f** FESEM image of $Ni_{1-X}Ag_XO$ (where $X = 0.0$, 0.01, 0.03, 0.05, 0.10, and 0.15) and the inset of this figures are the histogram (frequency vs average particle) with Gaussian fitting

particle size decreases gradually when the concentrations are increased further up to $X = 0.15$. This result is due that there may be some Ag^+ ions which have restricted the growth of NiO nanoparticle and hence the rate of nucleation of the NiO nanoparticle decreases gradually [57]. The increase in agglomeration of the particles with the increase in the concentrations of the dopant is due to increase of the surface charges with doping which attracts

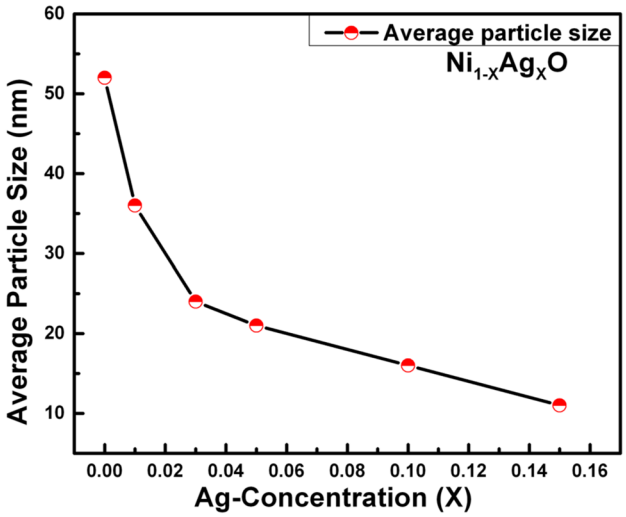

Fig. 3 Variation of the average particle size with the concentration (*X*) of $Ni_{1-X}Ag_XO$ (where $X = 0.0$, 0.01, 0.03, 0.05, 0.10, and 0.15)

the particles and coagulates the particles through Van der Waals forces [64–66].

Figure 4a–b shows the variation of the standard deviation of the particle size distributions with the concentration of Ag and average particle size. The standard deviation is calculated by taking the half of the full-width half maxima (FWHM) of Gaussian fitted curve. Figure 4 shows that the standard deviation nearly inversely depends on the concentration and directly on the particle size [67–69]. This appreciable increase in the standard deviation of the distribution with the particle size clearly indicates that the broadening of the particle size distributions increases as the agglomeration of particles increases with increase in Ag-doping content.

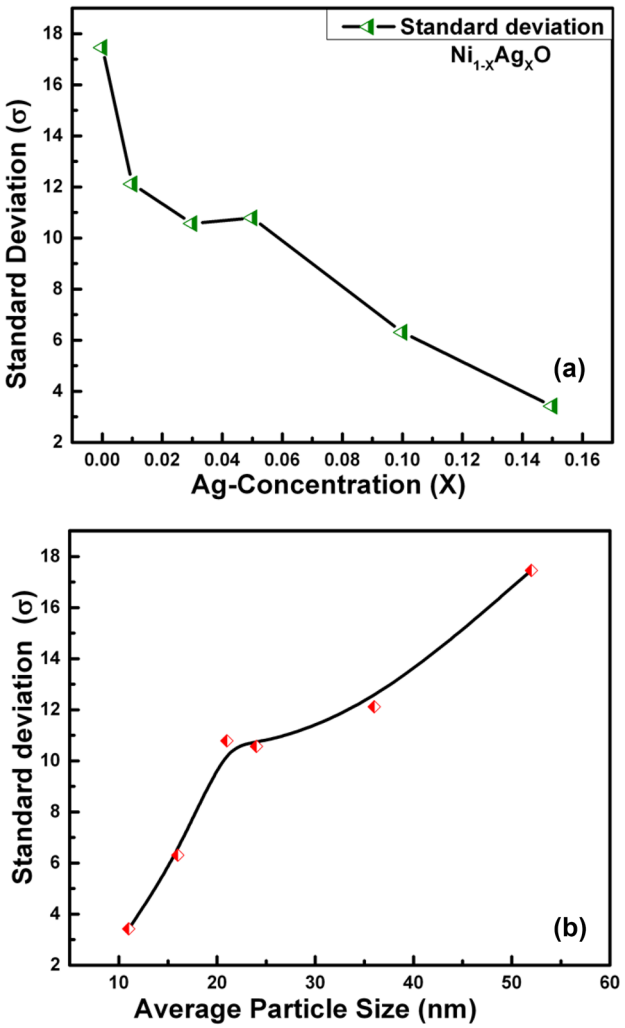

Fig. 4 **a** Plot between standard deviation and Ag Concentration (*X*) of $Ni_{1-X}Ag_XO$ (where $X = 0.0$, 0.01, 0.03, 0.05, 0.10, and 0.15), **b** plot between standard deviation and average particle size

3.3 UV–Visible spectroscopy

Figure 5 shows the UV–Visible spectrum of NiO nanoparticles. This shows that the absorbance peak is broad and stronger in the UV region. The optical bandgap is calculated with the help of Tau equation given below:

$$(\alpha h\nu) = A\left(h\nu - E_g\right)^{1/p} \tag{1}$$

and

$$\alpha = \frac{2.303 * A}{t} \tag{2}$$

where α is the absorbance coefficient and calculated with the help of Eq. (2). *A, t, h,* E_g, and ν are absorbance, the width of a cuvette, Planck's constant (4.135667×10^{-15} eV), the optical band gap, and the transition frequency, respectively. The value of p is based on the type of optical transitions. The value of p can be used 1/2, 3/2, 2 and 3/2 which means direct allowed, direct forbidden, indirect allowed and indirect forbidden bands, respectively [41]. The inset of Fig. 5 shows the Tau plot of pure NiO sample. The calculated optical band gap of the pure NiO sample is 3.70 eV which is less than the reported value 4.42 eV of near-stoichiometric NiO nanoparticles [32, 70–72]. This reduction in band gap is due to the creation of lattice defects such as oxygen vacancies, Ni and Ag interstitials as reported [73–75]. The lattice defects created in the materials result in the formation of new electronic states in the forbidden gap and hence lead to the reduction in the band gap energy [76].

Figure 6a–b show the UV–Visible spectra and Tau plots, respectively, for the samples with $X = 0.1$, 0.03, 0.05, 0.10, and 0.15. The transmittance in the visible-light range is sensitive to the particle size as well as agglomeration [77]. Figure 6a shows the decrease in the transmittance with

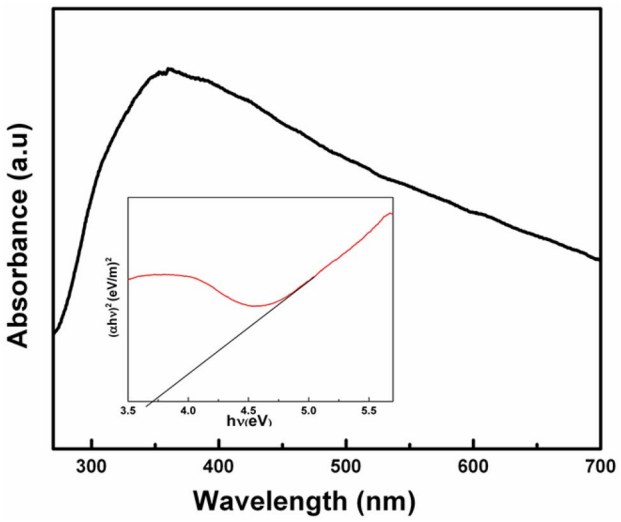

Fig. 5 Absorbance spectrum of the pure NiO sample and inset shows the tau plot of the NiO

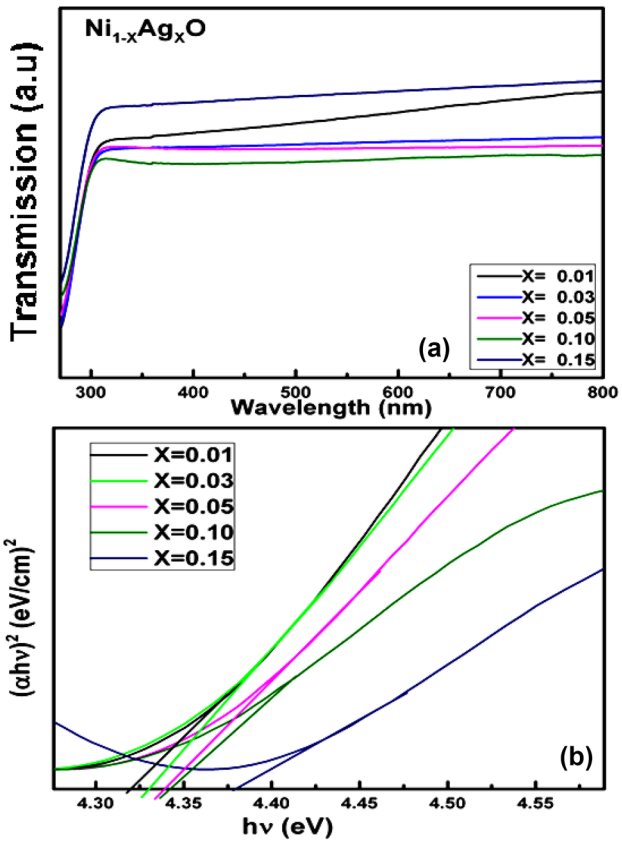

Fig. 6 **a** Absorbance spectrum of the $Ni_{1-X}Ag_XO$ (where $X=0.0$, 0.01, 0.03, 0.05, 0.10, and 0.15). **b** Optical band gap of the $Ni_{1-X}Ag_XO$ (where $X=0.0$, 0.01, 0.03, 0.05, 0.10, and 0.15) at different Ag concentration

the increase of Ag-doping content up to $X=0.10$, which is the clear indication of the increase in agglomeration. The absorbance peak shifted to the lower wavelength side which indicates the blue shift in the band gap. The calculated optical band gap using Tau plot also shows that it increases from 3.70 to 4.38 eV when the X is increased from 0.0 to 0.15 (see Fig. 7) as also reported in case of Ag-doped NiO thin films [57]. The band gap increases rapidly as the concentration of Ag increases up to $X=0.01$. But, after that band gap changes slowly. The increase in band gap can be explained due to the quantum size effect [28]. The average particle size decreases with the increase in Ag content. Therefore, the band gap increases with the decrease in average particle size. But, the decrease in band gap is only 18% as average particle size changes from 11 to 52 nm (nearly 4 times increase in particle size). It is reported in the literature that the band gap of NiO decreases from 3.86 to 3.47 eV as particle size is increased from 40 to 70 nm [78]. Therefore, such a small variation in band gap with the decrease in particle size in case of Ag-doped NiO nanoparticles cannot be explained completely using dominating quantum size effect at the nanoscale. The XRD and FESEM analysis confirm that the oxygen vacancies increase with the increase in Ag-doping content due to the crystal distortion occurred due to the substitution of silver in NiO lattice. As an effect, Ag^+ doping in NiO is stabilized by the creation of Ni^{3+} ions due to the conversion of Ni^{2+} ions which produces the formation of oxygen vacancy in the lattice of NiO. These oxygen vacancies lead

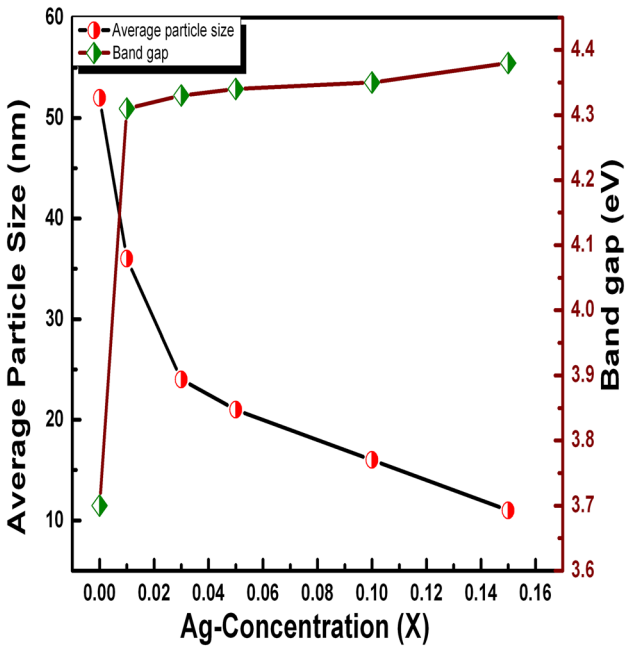

Fig. 7 Variation of band gap and average particle size with the concentration (X) of $Ni_{1-X}Ag_XO$ (where $X=0.0$, 0.01, 0.03, 0.05, 0.10, and 0.15)

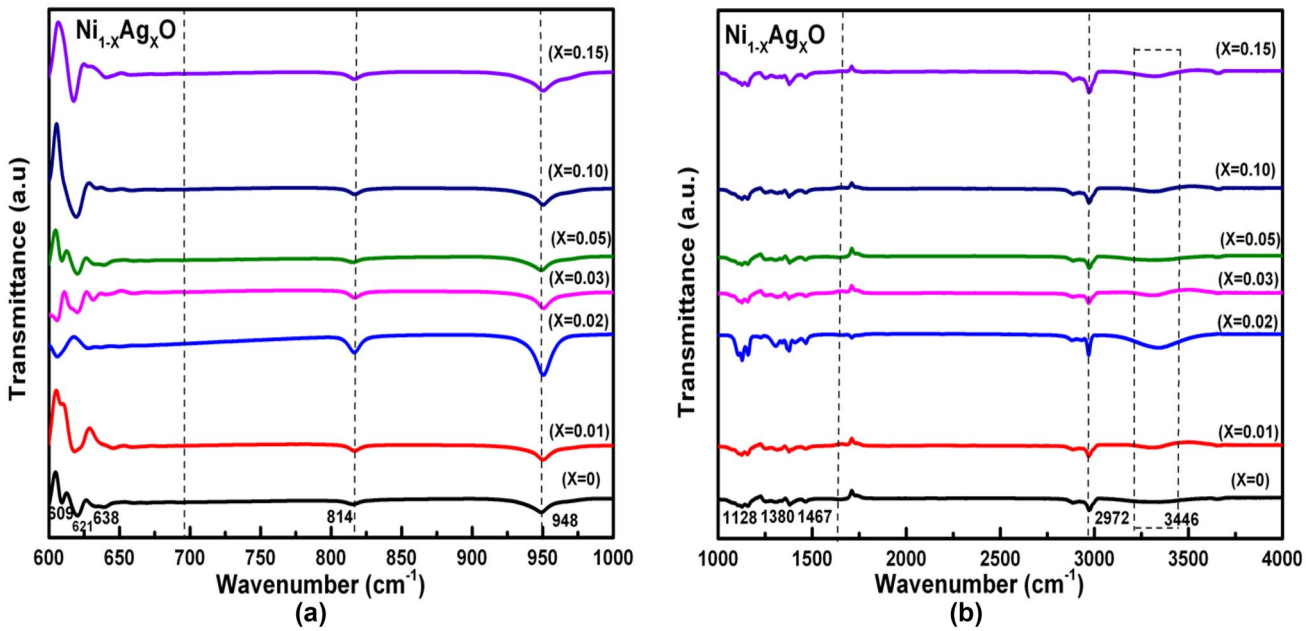

Fig. 8 **a** FT–IR spectra of $Ni_{1-X}Ag_XO$ (where $X=0.0$, 0.01, 0.03, 0.05, 0.10, and 0.15) as the function of wavenumber (cm^{-1}) in the range of 600–1000 cm^{-1}. **b** FT–IR spectra of $Ni_{1-X}Ag_XO$ (where $X=0.0$, 0.01, 0.03, 0.05, 0.10, and 0.15) as the function of wavenumber (cm^{-1}) in the range of 1000–4000 cm^{-1}

to decrease in the optical band gap as reported in the literature [79, 80]. Therefore, the opposite effects of oxygen vacancies on the band gap compared to dominating quantum size effect lead to only a small increase in band gap with the increase in Ag-doping in NiO. The refractive index is calculated using Moss relation, $n = \left(108/E_g\right)^{1/4}$ [81]. The calculated refractive index for the pure NiO is 2.324 which is more than the literature value (2.227) [81]. The refractive index are 2.284, 2.274, 2.271, 2.268, and 2.266 for $X=0.01$, 0.03, 0.05, 0.10 and 0.15, respectively.

3.4 FT–IR analysis

Figure 8a, b shows the FTIR spectra of the $Ni_{1-X}Ag_XO$ (where $X=0$, 0.01, 0.02, 0.03, 0.05, 0.10 and 0.15) samples. The peaks appear from 600 to 700 cm^{-1} is due to the Ni–O and Ag–O bond stretching, which clearly indicates the formation of the Ag-doped NiO phase [81, 82] (see Fig. 8a). Peaks at 814 and 948 cm^{-1} appear due to the epoxy group present in the citric acid [83]. The peaks appearing at 1128, 1380 and 1467 cm^{-1} is due to C–O,CO_3^{2-} and the carboxylate group, respectively (see Fig. 8b). The peaks at 2972, 3446 cm^{-1} are due to the CH_2 present in the precursor and O–H stretching vibration, respectively [84]. The intensity of these peaks appeared from 600 to 700 cm^{-1} is increasing as the Ag-doping concentration increases.

4 Conclusions

The single-phase and oxygen-deficient $Ni_{1-X}Ag_XO$ (where $X=0.0$, 0.05, 0.10) nanoparticles are synthesized. It is found that the formation of lattice defects such as O^{2-} vacancies and Ag nanoclusters in lattice sites reduces the unit cell volume as the concentration of Ag-dopant increase in NiO lattice. Ag-doping also inhibits the growth of NiO. The creation of disorder due to the formation of lattice defects leads to increase in strain with the increase in Ag-doping content. The increase in nonuniformity in particle size distributions is observed with increase in Ag-doping content. A small increase in the optical band gap with an increase in Ag content is also reported. The increase in oxygen vacancy leads to decrease in the band gap, but the opposite is the effect of the size of nanoparticles. Therefore, this small change in band gap is explained on the basis of the combined effect of lattice defects and the quantum confinement effect. FT–IR confirms the presence of Ni-O and Ag-O bonding in the samples. The prepared nanoparticles can be used in the semiconductor industry in optoelectronic devices due to its wide band gap.

Acknowledgements One of the authors (Rohit Sharma) is grateful to the Central Instrumentation Laboratory (CIL) and Department of Physical Sciences, Central University of Punjab, Bathinda for providing the research facilities. Authors are also thankful to the Thaper University, Patiala, for the XRD characterization. Rohit Sharma would also like to acknowledge Nilesh Saykr and Anil Arya for their help in plotting the graphs.

References

1. R.S. Devan, R.A. Patil, J.H. Lin, Y.R. Ma, One-dimensional metal-oxide nanostructures: recent developments in Synthesis, characterization, and applications. Adv. Funct. Mater. **22**(16), 3326–3370 (2012)
2. K. Karthik, G.K. Selvan, M. Kanagaraj, S. Arumugam, N.V. Jaya, Particle size effect on the magnetic properties of NiO nanoparticles prepared by a precipitation method. J. Alloy Compd. **509**(1)), 181–184 (2011)
3. G. Singh, D. Jalandhara, K. Yadav, Effect of grain size on optical properties of iron oxide nanoparticles. AIP Conf. Proc. **1728**(1), 020409 (2016) **(1–4)**
4. N. Bhardwaj, A. Gaur, K. Yadav, Effect of doping on optical properties in $BiMn_{1-x}(TE)_xO_3$ (where $x = 0.0$, 0.1 and TE = Cr, Fe, Co, Zn) nanoparticles synthesized by microwave and sol–gel methods. Appl. Phys. A **123**, 429 (2017) **(1–7)**
5. A. Kumar, K. Yadav, Optical properties of nanocrystallites films of α-Fe_2O_3 and α-$Fe_{2-x}Cr_xO_3$ ($0.0 \leq x \leq 0.9$) deposited on glass substrates. Mater. Res. Express **4**, 075003 (2017) **(1–11)**
6. C.R.H. Bahl, The magnetic properties of antiferromagnetic nanoparticles: NiO and Fe_2O_3. Risø National Laboratory. (Risø-PhD; No. 30(EN)) (2006)
7. S.P. Walch, W.A. Goddard III, Electronic states of the nickel oxide molecule. J. Am. Chem. Soc. **100**(5), 1338–1348 (1978)
8. R. Newman, R.M. Chrenko, Optical properties of nickel oxide. Phys. Rev. **114**, 1507–1513 (1959)
9. A. Rostamnejadi, S. Bagheri, Optical, magnetic, and microwave properties of Ni/NiO nanoparticles. Appl. Phys. A **123**, 233 (2017) **(1–9)**
10. M. Carbone, E. M.a Bauer, L. Micheli, M. Missori, NiO morphology dependent optical and electrochemical properties. Colloids Surf. A **532**, 178–182 (2017)
11. N.M. Hosny, Synthesis, characterization and optical band gap of NiO nanoparticles derived from anthranilic acid precursors via a thermal decomposition route. Polyhedron **30**, 470–476 (2011)
12. A.G. Al-Sehemi, A.S. Al-Shihri, A. Kalam, G. Du, T. Ahmad, Microwave synthesis, optical properties and surface area studies of NiO nanoparticles. J. Mol. Struct. **1058**, 56–61 (2014)
13. S.A. Makhlouf, M.A. Kassem, M.A. Abdel-Rahim, Crystallite size-dependent optical properties of nanostructured NiO films. Optoelectron Adv. Mat. **4**(10), 1562–1567 (2010)
14. W.J. Duan, S.H. Lu, Z.L. Wu, Y.S. Wang, Size effects on properties of NiO nanoparticles grown in alkali salts. J. Phys. Chem. C **116**, 26043–26051 (2012)
15. A. Kalam, A.S. Al-Shihri, M. Shakir, A.A. El-Bindary, S.S. El, G. Yousef, Du, Spherical NiO nanoparticles (SNPs): synthesis, characterization, and optical properties. Synth. React. Inorg. Metal-Org. Nano-Metal Chem. **41**(10), 1324–1330 (2011)
16. G. Natu, P. Hasin, Z. Huang, Z. Ji, M. He, Y. Wu, Valence band-edge engineering of nickel oxide nanoparticles via cobalt doping for application in p-type dye-sensitized solar cells. ACS Appl. Mater. Interfaces **4**(11), 5922–5929 (2012)
17. D. Chen, F. Deng, C. Ding, Y. Wang, H. Li, An Nb-doped nickel oxide–carbon nanotubes composite-enhanced electrochemical DNA biosensor for detection of Lead (II) Ion. Int. J. Electrochem. Sci **10**(11), 9015–9027 (2015)
18. J. Jia, F. Luo, C. Gao, C. Suo, X. Wang, H. Song, X. Hu, Synthesis of La-doped NiO nanofibers and their electrochemical properties as electrode for supercapacitors. Ceram Int **40**(5), 6973–6977 (2014)
19. P. Muthukumaran, C.V. Raju, C. Sumathi, G. Ravi, D. Solairaj, P. Rameshthangam, S. Alwarappan, Cerium doped nickel-oxide nanostructures for riboflavin biosensing and antibacterial applications. New J. Chem. **40**(3), 2741–2748 (2016)
20. J. Li, R. Yan, B. Xiao, D.T. Liang, D.H. Lee, Preparation of nano-NiO particles and evaluation of their catalytic activity in pyrolyzing biomass components. Energy Fuels **22**(1), 16–23 (2007)
21. Y. Yao, J. Zhang, Z. Wei, A. Yu, Hydrothermal synthesis of porous NiO nanosheets and application as anode material for lithium ion batteries. Int. J. Electrochem. Sci **7**, 1433–1442 (2012)
22. P. Lunkenheimer, A. Loidl, C.R. Ottermann, K. Bange, Correlated barrier hopping in NiO films. Phys. Rev. B **44**(11), 5927 (1991)
23. H.P. Rooksby, Structure of nickel oxide. Nature **152**(3854), 304 (1943)
24. R.W. Cairns, E. Ott, X-ray studies of the system nickel—oxygen—water. I. Nickelous oxide and hydroxide. J. Am. Chem. Soc. **55**(2), 527–533 (1933)
25. M. Oliver, S.C. Parker, W.C. Mackrodt, Computer simulation of the crystal morphology of NiO. Model. Simul. Mater. Sci. Eng. **1**(5), 755 (1993)
26. H. Sato, T. Minami, S. Takata, T. Yamada, Transparent conducting p-type NiO thin films prepared by magnetron sputtering. Thin Solid Films **236**(1), 27–33 (1993)
27. D. Adler, J. Feinleib, Electrical and optical properties of narrow-band materials. Phys. Rev. B **2**(8), 3112–3134 (1970)
28. S. D.Varshney, Dwivedi, Synthesis, structural, Raman spectroscopic and paramagnetic properties of Sn doped NiO nanoparticles. Superlattices Microstruct. **86**, 430–437 (2015)
29. S.M. Meybodi, S.A. Hosseini, M. Rezaee, S.K. Sadrnezhaad, D. Mohammadyani, Synthesis of wide band gap nanocrystalline NiO powder via a sonochemical method. Ultrason Sonochem. **19**(4), 841–845 (2012)
30. P. Jeevanandam, Y. Koltypin, A. Gedanken, Synthesis of nanosized α-nickel hydroxide by a sonochemical method. Nano Lett. **1**(5), 263–266 (2001)
31. Y. Wu, Y. He, T. Wu, T. Chen, W. Weng, H. Wan, Influence of some parameters on the synthesis of nanosized NiO material by modified sol–gel method. Mater Lett **61**(14), 3174–3178 (2007)
32. M. Alagiri, S. Ponnusamy, C. Muthamizhchelvan, Synthesis and characterization of NiO nanoparticles by sol–gel method. J. Mater. Sci. Mater. Electron **23**(3), 728–732 (2012)
33. N.N.M. Zorkipli, N.H.M. Kaus, A.A. Mohamad, Synthesis of NiO Nanoparticles through sol–gel Method. Procedia Chem. **19**, 626–631 (2016)
34. A.S. Danial, M.M. Saleh, S.A. .Salih, M.I. Awad, On the synthesis of nickel oxide nanoparticles by sol–gel technique and its electrocatalytic oxidation of glucose. J. Power Sources **293**, 101–108 (2015)
35. A. Rahdar, M. Aliahmad, Y. Azizi, NiO nanoparticles: synthesis and characterization. J Nanostruct. **5**(2), 145–151 (2015)
36. Y. Du, W. Wang, X. Li, J. Zhao, J. Ma, Y. Liu, G. Lu, Preparation of NiO nanoparticles in microemulsion and its gas sensing performance. Mater. Lett. **68**, 168–170 (2012)
37. Y. Chen, D.L. Peng, D. Lin, X. Luo, Preparation and magnetic properties of nickel nanoparticles via the thermal decomposition of nickel organometallic precursor in alkylamines. Nanotechnology **18**(50), 505703 (2007)
38. T. Takei, J. Suenaga, T. Ishida, M. Haruta, Ethanol oxidation in water catalyzed by gold nanoparticles supported on NiO doped with Cu. Top. Catal. **58**(4–6), 295–301 (2015)
39. G. Allaedini, P. Aminayi, S.M. Tasirin, Structural properties and optical characterization of flower-like Mg doped NiO. AIP Adv. **5**(7), 077161 (2015)
40. W. Guo, K.N. Hui, K.S. Hui, High conductivity nickel oxide thin films by a facile sol–gel method. Mater. Lett. **92**, 291–295 (2013)
41. A. Alshahrie, I.S. Yahia, A. Alghamdi, P.Z. Al Hassan, Morphological, structural and optical dispersion parameters of Cd-doped NiO nanostructure thin film. Optik-Int. J. Light Electron Opt. **127**(12), 5105–5109 (2016)

42. K.O. Moura, R.J.S. Lima, C.B.R. Jesus, J.G.S. Duque, C.T. Meneses, Fe-doped NiO nanoparticles: synthesis, characterization, and magnetic properties. Revista Mexicana de Fisica S **58**(2), 167–170 (2012)
43. S. Layek, H.C. Verma, Room temperature ferromagnetism in Mn-doped NiO nanoparticles J. Magn. Magn. Mater. **397**, 73–78 (2016)
44. Z. Halem, N. Halem, M. Abrudeanu, S. Chekroude, C. Petot, G. Petot-Ervas, Transport properties of Al or Cr-doped nickel oxide relevant to the thermal oxidation of dilute Ni-Al and Ni-Cr alloys. Solid State Ionics **297**, 13–19 (2016)
45. J. Wang, Z. Wang, B. Huang, Y. Ma, Y. Liu, X. Qin, Y. Dai, Oxygen vacancy induced band-gap narrowing and enhanced visible light photocatalytic activity of ZnO. ACS Appl. Mater. Interfaces **(8)**, 4024–4030 (2012)
46. X. Han, N. Amrane, Z. Zhang, M. Benkraouda, Oxygen Vacancy Ordering and Electron Localization in CeO_2: Hybrid Functional Study. J. Phys. Chem. C **120**(25), 13325–13331 (2016)
47. S. Park, H. Kheel, G.-J. Sun, S.K. Hyun, S.E. Park, C. Lee, Ethanol sensing properties of Au-functionalized NiO nanoparticles. Bull. Korean Chem. Soc. **37**, 713–719 (2016)
48. Z. Jiang, J. Xie, D. Jiang, X. Wei, M.Chen, Modifiers-assisted formation of nickel nanoparticles and their catalytic application to p-nitrophenol reduction. Cryst. Eng. Comm. **15**(3), 560–569 (2013)
49. Y. Zhang, The first observation of Ni and Ni_2O_3 phases in the sol–gel Ag-doped NiO film. Synth. React. Inorg. Metal-Org. Nano-Metal Chem. **46**, 1565–1570 (2016)
50. O. Volnianska, P. Boguslawski, J. Kaczkowski, P. Jakubas, A. Jezierski, E. Kaminska, Theory of doping properties of Ag acceptors in ZnO. Phys. Rev. B **80**, 245212 (2009) **(1–8)**
51. P. Amornpitoksuk, S. Suwanboon, S. Sangkanu, A. Sukhoom, N. Muensit, J. Baltrusaitis, Synthesis, characterization, photocatalytic and antibacterial activities of Ag-doped ZnO powders modified with a diblock copolymer. Powder Technol. **219**, 158–164 (2012)
52. T.X.T. Sayle, S.C. Parker, C.R.A. Catlow, The role of oxygen vacancies on ceria surfaces in the oxidation of carbon monoxide. Surf. Sci. **316**(3), 329–336 (1994)
53. L.E. Depero, A. Marino, B. Allieri, E. Bontempi, L. Sangaletti, C. Casale, M. Notaro, Morphology and microstructural properties of TiO_2 nanopowders doped with trivalent Al and Ga cations. J. Mater. Res. **15**(10), 2080–2086 (2000)
54. X.S. Cui, *The Basic Theory of Solid Chemistry*. (Beijing Institute of Technology Printing, Beijing, 1991)
55. Y. Liu. C.Y. Liu, Q.H. Rong, Z. Zhang, Characteristics of the silver-doped TiO_2 nanoparticles. Appl. Surf. Sci. **220**(1)), 7–11 (2003)
56. N. Agasti, N.K. Kaushik, One pot synthesis of crystalline silver nanoparticles. A. J. Mater. **2**(1), 4–7 (2014)
57. M.M.A. Hussein, Optical and structural characteristics of NiO thin films doped with AgNPs by sputtering method. INAE Lett. **2**, 35–39 (2017)
58. P.Y. Yang, F. Zeng, F. Pan, Exchange bias and training effect in Ni/Ag-doped NiO bilayers. J. Magn. Magn. Mater. **322**(5), 542–547 (2010)
59. A.A. Akl, A.S. Hassanien, Microstructure and crystal imperfections of nanosized CdS_xSe_{1-x} thermally evaporated thin films. Superlattices Microstruct. **85**, 67–81 (2015)
60. M.B. Dutt, R. Banerjee, A.K. Barua, Transport properties of Lithium and Sodium doped Nickel oxide. Phys. Status Solidi (a) **65**(1), 365–370 (1981)
61. W. Qin, T. Nagase, Y. Umakoshi, J.A. Szpunar, Relationship between microstrain and lattice parameter change in nanocrystalline materials. Philos. Mag. Lett. **88**(3), 169–179 (2008)
62. M. Yang, H. Pu, Q. Zhou, Q. Zhang, Transparent p-type conducting K-doped NiO films deposited by pulsed plasma deposition. Thin Solid Films **520**, 5884–5888 (2012)
63. A.M. El-Shabiny, G.A. El-Shobaky, I.F. Hewaidy, A.A. Ramadan, Microstrain and lattice parameter of pure and Li_2O-doped nickel oxide solid. Cryst. Res. Technol. **23**(7), 911–917 (1988)
64. A. Henglein, Reactions of organic free radicals at colloidal silver in aqueous solution. Electron pool effect and water decomposition. J. Phys. Chem. **83**(17), 2209–2216 (1979)
65. S. Tsunekawa, K. Ishikawa, Z.Q. Li, Y. Kawazoe, A. Kasuya, Origin of anomalous lattice expansion in oxide nanoparticles. Phys. Rev. Lett. **85**(16), 3440–3443 (2000)
66. P. Bindu, S. Thomas, Estimation of lattice strain in ZnO nanoparticles: X-ray peak profile analysis. J. Theor. Appl. Phys. **8**(4), 123–134 (2014)
67. D. Mott, J. Galkowski, L. Wang, J. Luo, C.-J. Zhong, Synthesis of Size-Controlled and Shaped Copper Nanoparticles. Langmuir **23**, 5740–5745 (2007)
68. S. Hong, X. Li, Optimal size of gold nanoparticles for surface-enhanced raman spectroscopy under different conditions. J Nanomater. **2013**, 790323 (2013) **(1–9)**
69. D. Coleman, L. Vanatta statistics in analytical chemistry: part 14—calibration example 4. (2004) http://www.americanlaboratory.com/913-Technical-Articles/1688-Statistics-in-Analytical-Chemistry-Part-14-Calibration-Example-4/. Accessed 17 Dec 2004
70. R. Vasan, F. Gao, M.O. Manasreh, C.D. Heyes, Investigation of charge transport between nickel oxide nanoparticles and CdSe/ZnS alloyed nanocrystals. MRS Adv. Mater. Res. Soc. (2017) https://doi.org/10.1557/adv.2017.488
71. A.J. Varkey, A.F. Fort, Solution growth technique for deposition of nickel oxide thin films. Thin Solid Films **235**, 47–50 (1993)
72. X. Wang, J. Song, L. Gao, J. Jin, H. Zheng, Z. Zhang, Optical and electrochemical properties of nanosized NiO via thermal decomposition of nickel oxalate nanofibres. Nanotechnol **16**(1), 37–39 (2004)
73. R. Vasan, H. Salman, M.O. Manasreh, All inorganic quantum dot light emitting devices with solution processed metal oxide transport layers. MRS Adv. **1**, 305–310 (2016)
74. S. Liu, R. Liu, Y. Chen, S. Ho, H. Jong, J.H. Kim, F. So, Nickel oxide hole injection/transport layers for efficient solution-processed organic light-emitting diodes. Chem. Mater. **26**, 4528–4534 (2014)
75. F. Mehmood, R. Pachter, N.R. Murphy, W.E. Johnson, C.V. Ramana, Effect of oxygen vacancies on the electronic and optical properties of tungsten oxide from first principles calculations. J. Appl. Phys. **120**, 233105 (2016)
76. L. Kumari, W.Z. Li, C.H. Vannoy, R.M. Leblanc, D.Z. Wang, Vertically aligned and interconnected nickel oxide nanowalls fabricated by hydrothermal route. Cryst. Res. Technol. **44**, 495–499 (2009)
77. T. Tsuzuki, J.S. Robinson, P.G. Mccormick, UV-shielding ceramic nanoparticles synthesised by mechanochemcial processing. J. Am. Ceram. Soc. **38**(1), 15–19 (2002)
78. V. Patil, S. Pawar, M. Chougule, P. Godse, R. Sakhare, S. Sen, P. Joshi, Effect of annealing on structural, morphological, electrical and optical studies of nickel oxide thin films. J. Surf. Eng. Mater. Adv. Technol. **1**, 35–41 (2011)
79. N. Peijiang, Y. Jinliang, M. Delan, The effects of N-doping and oxygen vacancy on the electronic structure and conductivity of $PbTiO_3$. Semicond. Sci. Technol **36**(4), 043004 (2015) **(1–6)**
80. M.M. El-Nahass, H.S. Soliman, A. El-Denglawey, Absorption edge shift, optical conductivity, and energy loss function of nano thermal-evaporated N-type anatase TiO_2 films. Appl. Phys. A **122**(8), 775 (2016) **(1–10)**

81. R.R. Reddy, Y.N. Ahammed, A study on the Moss relation. Infrared Phys. Technol. **36**(5), 825–830 (1995)
82. A.N. Abd, R.S. Ali, A.A. Hussein, Fabrication and characterization of nickel oxide nanoparticles/silicon heterojunction. J. Multidiscip. Eng. Sci. Studies **2**(4), 434–440 (2016)
83. M.S. Hossan, M.A. Rahman, M.R. Karim, M.A. Miah, H. Ahmad, Preparation of epoxy functionalized hybrid nickel oxide composite polymer particles. Am. J. Polym. Sci. **3**(5), 83–89 (2013)
84. M. Vivek, P.S. Kumar, S. Steffi, S. Sudha, Biogenic silver nanoparticles by Gelidiella acerosa extract and their antifungal effects. Avicenna J Med Biotechnol. **3**(3), 143–148 (2011)